

Electrical switching of spin-polarized light-emitting diodes based on a 2D CrI₃/hBN/WSe₂ heterostructure

Received: 18 April 2024

Accepted: 5 August 2024

Published online: 09 August 2024

 Check for updatesJianchen Dang¹, Tongyao Wu¹, Shaohua Yan^{2,3}, Kenji Watanabe⁴, Takashi Taniguchi⁵, Hechang Lei^{2,3} & Xiao-Xiao Zhang¹✉

Spin-polarized light-emitting diodes (spin-LEDs) convert the electronic spin information to photon circular polarization, offering potential applications including spin amplification, optical communications, and advanced imaging. The conventional control of the emitted light's circular polarization requires a change in the external magnetic field, limiting the operation conditions of spin-LEDs. Here, we demonstrate an atomically thin spin-LED device based on a heterostructure of a monolayer WSe₂ and a few-layer antiferromagnetic CrI₃, separated by a thin hBN tunneling barrier. The CrI₃ and hBN layers polarize the spin of the injected carriers into the WSe₂. With the valley optical selection rule in the monolayer WSe₂, the electroluminescence exhibits a high degree of circular polarization that follows the CrI₃ magnetic states. Importantly, we show an efficient electrical tuning, including a sign reversal, of the electroluminescent circular polarization by applying an electrostatic field due to the electrical tunability of the few-layer CrI₃ magnetization. Our results establish a platform to achieve on-demand operation of nanoscale spin-LED and electrical control of helicity for device applications.

The spin states of materials are the building blocks of modern information technology. Most spintronics devices achieve the control and detection of electronic spin based on electrical currents. In a spin-polarized light-emitting diode (spin-LED), the injection of spin-polarized carriers results in circularly polarized electroluminescence (EL), interfacing optoelectronics and photonics with spintronics¹. Spin-LEDs have been demonstrated using GaAs-based ferromagnet/semiconductor structures^{2–4}, organic semiconductors like chiral molecules⁵ and hybrid perovskites⁶, and two-dimensional (2D) layered heterostructures^{7,8}, with some showing capabilities of room-temperature operation. However, controlling the degree of polarization in the EL signals for these spin-LED devices often requires a change in the temperature, magnetic field, or chemical composition. Efficient

electrical control of the EL polarization will enable low-power and high-speed applications in spin-optoelectronics¹, information processing⁹, and ellipsometry-based tomography^{10,11}.

The recent advances in 2D layered materials open up possibilities for optoelectronics and spintronics device designs that are more flexible and tunable. In a monolayer semiconducting transition metal dichalcogenide (TMD), the valley-spin coupling and the valley-dependent optical selection rule ensure that we can selectively determine the circular polarization of the emitted light based on the carriers' and excitons' valley and spin occupation¹². In addition, 2D TMDs have remarkable optical properties due to their large excitonic interactions, and their optoelectronic prototypes like photodetector and light-emitting diodes have been demonstrated¹³. The van der

¹Department of Physics, University of Florida, Gainesville, FL, USA. ²Department of Physics and Beijing Key Laboratory of Opto-electronic Functional Materials & Micro-nano Devices, Renmin University of China, 100872 Beijing, China. ³Key Laboratory of Quantum State Construction and Manipulation (Ministry of Education), Renmin University of China, 100872 Beijing, China. ⁴Research Center for Functional Materials, National Institute for Materials Science, 1-1 Namiki, Tsukuba, Japan. ⁵International Center for Materials Nanoarchitectonics, National Institute for Materials Science, 1-1 Namiki, Tsukuba, Japan.

✉ e-mail: xxzhang@ufl.edu

Waaals magnetic crystals have been shown to maintain magnetic ordering down to monolayer or few-layer limit, enabling the construction of nanoscale spintronic devices and easy integration with other 2D systems^{14,15}. In particular, CrI₃ crystals are A-type antiferromagnets at the few-layer limit, with the spin easy axis along the out-of-plane direction. For an even or odd layer number, the corresponding magnetic states in CrI₃ are overall ferromagnetic or antiferromagnetic. The magnetic interactions, including the magnetic resonance frequency, in few-layer CrI₃ can be efficiently tuned by either an out-of-plane electric field or doping density^{16–18}, providing a unique opportunity to develop electrically tunable magnetic devices.

Here, we fabricated 2D LED structures based on monolayer WSe₂/hBN/few-layer CrI₃, where the doping of WSe₂ and CrI₃ can be individually controlled by separate gating electrodes. The CrI₃/hBN serves as a spin-polarizing layer for carrier injection. We showed that the WSe₂ EL gained circular polarization due to the CrI₃ spin filtering and spin-valley coupling. The EL light helicity switches with the layer-dependent magnetization in CrI₃. A large EL helicity of ~40% was achieved in one of the devices, which infers a close-to-unity spin filtering efficiency. We also demonstrated an efficient electrostatic control of the EL helicity through the electrical control of the CrI₃ magnetization^{16,17}. Our results established a 2D spin-LED prototype with programmable electrical control of the helicity, which enables optoelectronic device designs with more tunable control and high-speed operation capabilities.

Results

EL characterization

The dual-gated device geometry is shown in Fig. 1a. The back gate V_{bg} and top gate V_{tg} are used to control the doping of CrI₃ and WSe₂, respectively. When at appropriate bias voltages and doping levels, p-type carriers are injected through the CrI₃/hBN into the n-doped monolayer WSe₂, which gives rise to WSe₂ electroluminescence signals. In order to maintain the spin polarization during the carrier injection, a thin hBN tunneling barrier (the thickness is confirmed with the atomic force microscope measurement, as shown in Supplementary Fig. 1) is used to overcome the impedance mismatch¹⁹ and also to avoid the Schottky barrier at the interfaces. Two graphite stripes contact the WSe₂ and CrI₃ separately and serve as the source and drain contacts. Fig. 1b shows the microscopic image of a device with a bilayer CrI₃. The Methods section provides detailed information on material preparation and heterostructure fabrication.

When applying a bias voltage between the CrI₃ and WSe₂, the tunneling current I starts to flow for both positive and negative applied bias voltages, as shown in Fig. 1d. The EL from the WSe₂ can only be observed for the positive bias region, and the onset EL threshold current decreases with an increasing top gate voltage, and therefore at a higher n-type doping density in WSe₂ (The back gate V_{bg} for the CrI₃ doping is kept at zero for this part of the experiment). Combined with the expected type-II band alignment between the WSe₂ and CrI₃²⁰ and

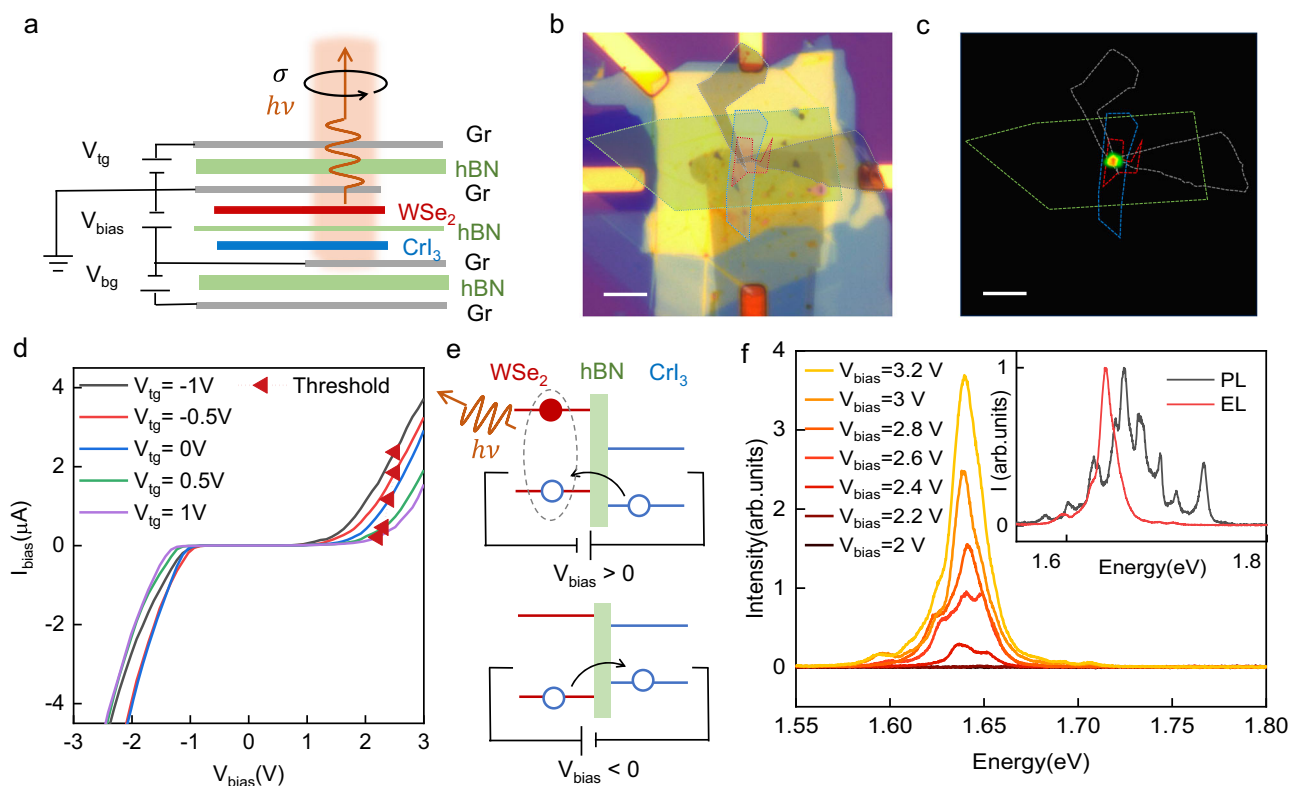


Fig. 1 | Electroluminescence based on WSe₂/hBN/CrI₃ heterostructure.

a Schematic of the device structure. The back gate V_{bg} and top gate V_{tg} are used to control the doping of CrI₃ and WSe₂. The bias voltage V_{bias} is applied across the vertical junction going through the hBN tunneling barrier. $h\nu$ indicates the emitted photon with circular polarization σ_{\pm} . **b** The whitelight microscopic image of a monolayer WSe₂/hBN/bilayer CrI₃ device. The scale bar is 10 μm . The monolayer WSe₂ is outlined by red dashed lines, blue dashed lines outline CrI₃, the thin hBN (~2.5 nm) tunneling layer is denoted by the green dashed lines, and the source and drain contacts (from graphite stripes) are denoted by the gray lines. **c** Spatially-resolved electroluminescence (EL) image of the device. The notation of dashed lines is the same as **b**. The scale bar is 10 μm . The EL signal comes from the

overlapped area of the source and drain contacts. **d** I–V characteristics of the heterostructure at different top gate voltages while keeping $V_{bg} = 0\text{ V}$. The red triangles denote the extracted threshold point for EL generation. **e** Band alignment schematics of the heterostructure under different bias voltages during EL generation with a positive V_{bias} (upper panel, WSe₂ n-doped) and no EL generation with a negative V_{bias} (lower panel). The arrows indicate the direction of carrier tunneling and the dashed ellipse represents the exciton. **f** EL spectra at different V_{bias} with $V_{tg} = 1\text{ V}$ and $V_{bg} = 0\text{ V}$. The inset shows the comparison of the normalized photoluminescence (PL) and EL spectra. The PL spectra was taken with a 633 nm continuous wave laser (10 μW). The EL spectrum was measured under $V_{bias} = 2.5\text{ V}$, $I_{bias} = 0.49\text{ }\mu\text{A}$ with $V_{tg} = 1\text{ V}$.

the measured doping level shift from the WSe₂ photoluminescence (PL) (see Supplementary Fig. 2), the *I*-*V* characteristic and the EL bias dependence can be understood by considering the type-II to type-I band alignment transition when applying a negative bias voltage, as depicted in Fig. 1e. With a positive bias voltage, p-type carriers flow from the CrI₃/hBN layer into WSe₂. They can recombine with the n-type carriers in WSe₂ and generate EL signals. On the other hand, with a negative bias voltage, there is no EL signal in WSe₂ when tuning the WSe₂ doping level from p- to n-type doping. It thus indicates that there is no carrier injection into WSe₂ with a negative V_{bias} (when there is significant tunneling current). This is likely due to the shift in CrI₃ bands under the bias voltage, which converts the type-II to a type-I band alignment. The p-type carriers can flow from WSe₂ to CrI₃ layers and give rise to tunneling currents without EL generation.

From the spatially-resolved EL imaging in Fig. 1c, the EL generation is most efficient at the overlapping region of the source and drain graphite strips, where the tunneling currents go through the vertical heterostructure without further diffusion or drift. Fig. 1f shows the evolution of the EL signals at different bias voltages and tunneling currents when $V_{\text{tg}} = 1$ V and $V_{\text{bg}} = 0$ V. The top gate dependence of the EL spectra is plotted in Supplementary Fig. 2a. The EL signal quenches when the WSe₂ is tuned to p-doped, which can be deduced from the gate-dependent PL in Supplementary Fig. 2b, consistent with the expected EL generation process in Fig. 1e. The *I*-*V* curves and EL spectra at different back gate voltages were summarized in Supplementary Fig. 2, which do not show significant back gate dependence. The comparison of the EL and PL (at $V_{\text{tg}} = 0$) spectra is plotted in the inset of Fig. 1f. The EL emission peak is redshifted with no obvious defect-related peaks, which may be attributed to the additional carrier screening and the charge-related defect states being filled up. A more detailed comparison and analysis of the EL exciton contributions can be found in Supplementary Fig. 3.

Spin-dependent circularly polarized EL

We measured the magnetic field-dependent EL to reveal the spin sensitivity of this structure. Under an out-of-plane magnetic field, the few-layer CrI₃ will go through layer-dependent spin-flip transitions. When the CrI₃ layer is spin-polarized, the CrI₃/hBN will serve as a spin-filtering layer for the injected holes into the WSe₂ layer. The valley-spin coupling and valley-dependent optical selection rule in WSe₂ subsequently generate circularly polarized light emission based on the injected hole spin polarization (Fig. 2a). The large spin-orbit coupling splitting in the WSe₂ valence bands and long valley lifetime of the holes further facilitate the generation of the circularly polarized EL. Fig. 2b shows the oppositely circularly polarized EL spectra at opposite magnetic fields from a bilayer CrI₃/hBN/WSe₂ device (± 1.8 T is a fully polarizing field for bilayer CrI₃). As shown in Fig. 2c, d, we measured and compared the magnetic state switching of the CrI₃ layer through the reflective magnetic circular dichroism (RMCD) and the EL light helicity switching with different magnetic field ramping directions. Here, the EL polarization is characterized by the helicity as defined by $(I_{\sigma^+} - I_{\sigma^-}) / (I_{\sigma^+} + I_{\sigma^-})$. The RMCD shows the spin-flip transition that corresponds to the layer-dependent spin switching in bilayer CrI₃²¹, as indicated by the schematic plot in Fig. 2c. The EL helicity follows the RMCD magnetic field dependence and shows a jump to $\pm 10\%$ at the spin-flip fields. This phenomenon was further confirmed by measuring three additional devices with bilayer CrI₃. In all cases, the EL helicity followed the RMCD traces (see Supplementary Fig. 4). As the temperature was increased to be close to the Neel temperature of CrI₃ (~ 45 K), the EL helicity also dropped to zero (see Supplementary Fig. 5).

Depending on the layer number of the CrI₃, we can further tune the EL helicity field dependence. A trilayer CrI₃ is ferromagnetic at zero fields and goes through layer dependent spin-flip transitions with an increasing out-of-plane magnetic field (Fig. 2e). The corresponding EL helicity of a trilayer CrI₃/hBN/WSe₂ device also shows zero field helicity

and spin-flip fields consistent with the RMCD signals, as shown in Fig. 2f. The measured EL helicity varies across different devices, possibly due to variations in device quality. We discussed the variability of EL helicity and present data for multiple bilayer and trilayer CrI₃ devices in Supplementary Table 1. The maximum saturation polarization obtained was $\sim 40\%$, as shown in this trilayer device. This helicity in EL is intrinsically limited mainly by the exciton depolarization, which arises from the efficient intervalley exciton exchange interactions²². Supplementary Fig. 7 is the measured circular polarization of neutral and charged excitons in PL with a near-resonant valley-polarized optical excitation, with trion states showing a maximum of $\sim 37\%$ circular polarization, close to the highest circular polarization observed in EL devices. We therefore infer the spin filter efficiency was close to unity with these 2D magnetic tunneling junctions in the device with observed maximum EL helicity, and the helicity was mostly constrained by the intervalley exciton depolarization.

Notably, the EL helicity is determined by the overall magnetization of the CrI₃, instead of the topmost layer adjacent to the WSe₂ layer, which is distinctly different from the previously reported circularly polarized PL quenching in CrI₃/WSe₂²³. In a CrI₃/WSe₂ structure, spin-dependent charge transfer is mostly determined by the adjacent CrI₃ layer spin polarization. In comparison, the hBN barrier here (Fig. 1a) ensures that the tunneling carriers' spin is set by the overall magnetization of the CrI₃ layer. The EL helicity does not show observable dependence on the WSe₂ layer doping level (Fig. 3a) and the applied bias voltage (Fig. 3b) within the EL generation ranges. These are consistent with the expectation of spin tunneling behavior, which is not sensitive to the relative shifts of Fermi levels across the heterostructure. To reveal the impact of the tunneling junction, we also measured EL signals with CrI₃/WSe₂ devices without the hBN tunneling barrier. While EL signals can still be observed, there is no obvious circular dichroism that depends on the CrI₃ magnetization (see Supplementary Fig. 6), which highlights the importance of tunneling barriers to reduce conductance mismatch and increase spin filter efficiency in 2D heterostructures.

To further illustrate the differences in the tunneling spin injection and spin-dependent charge transfer, we further compared the helicity of PL in a CrI₃/WSe₂ heterostructure and EL spectra in a CrI₃/hBN/WSe₂ device. Fig. 3d shows the circularly polarized PL taken with a linearly polarized excitation in CrI₃/WSe₂ under a 2 T magnetic field. The enhanced PL polarization is caused by charge transfer, consistent with previous work^{20,23}. In comparison, the EL polarization (Fig. 3c) is oppositely polarized. This is consistent with the expectation of the band alignments and transfer processes. During EL generation, the polarization is determined and aligned by the CrI₃ spin direction. As shown in Fig. 3e, injected spin-polarized carriers will reside in, e.g., the K valley because of the valley-spin coupling in monolayer TMD and gives rise to σ^+ emission. On the other hand, the PL polarization in a CrI₃/WSe₂ heterostructure arises from the spin-dependent charge transfer^{23,24}, which quenches the valley/spin-polarized exciton with carriers' spin aligned with the CrI₃ spin orientation. In the depicted scenario in Fig. 3f, under the same CrI₃ spin alignment as Fig. 3e, the K valley exciton will be quenched due to electron interlayer transfer, giving rise to an overall σ^- polarization in light emission.

Electrical switching of EL helicity

Efficient electrical tuning of magnetic interactions has been demonstrated in few-layer CrI₃ in prior studies^{16–18,25}. Here, we utilize the electrical tunability of CrI₃ to control the spin-dependent EL signals. To this end, we use the back gate to electrostatically tune the doping level in CrI₃ (Fig. 1a) while observing the EL helicity switching. When varying the doping in CrI₃, the spin-flip transition field can show significant shifting^{16,17} and gives rise to spin switching, and therefore EL helicity switching, at certain fixed magnetic fields. In Fig. 4a, we prepared a bilayer device in the “up” state by applying a

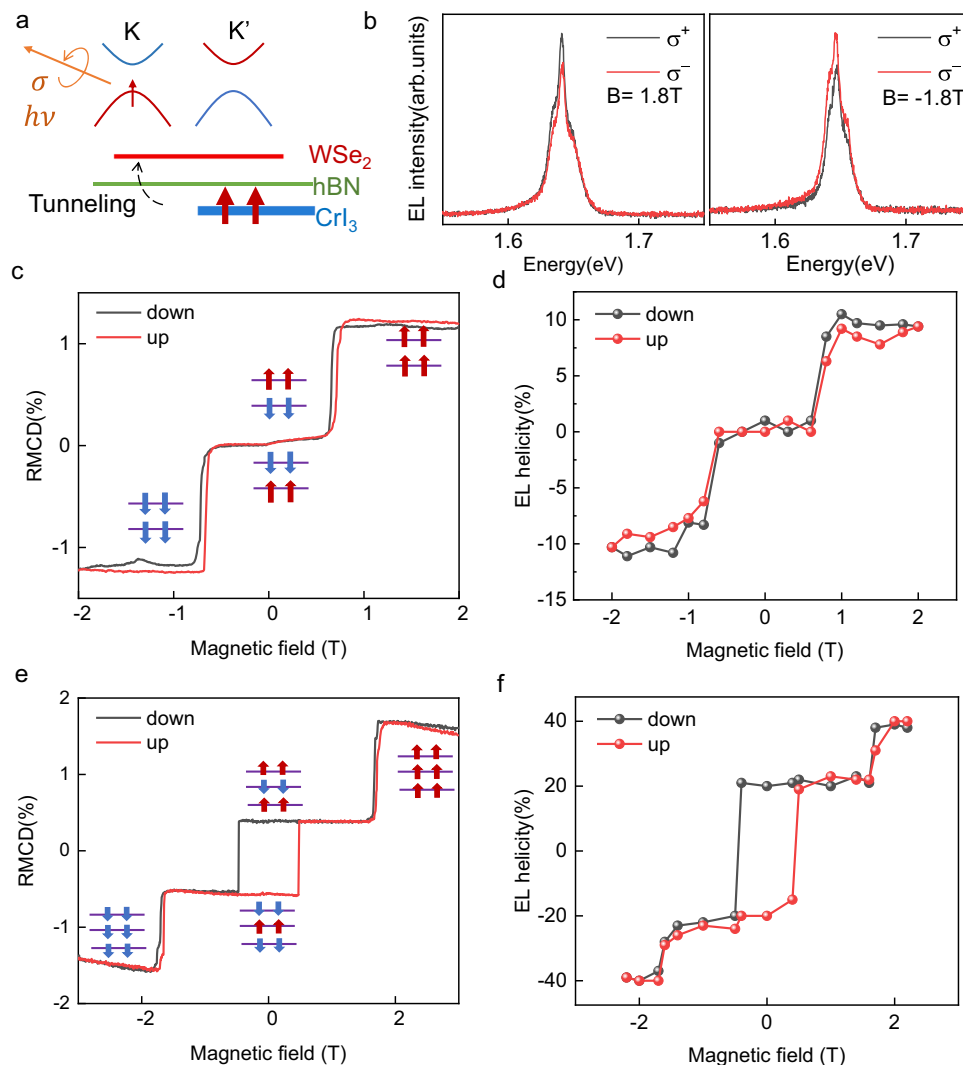


Fig. 2 | Spin-dependent EL. **a** The spin dependence in EL signals originated from the spin-polarized carrier injection through CrI₃/hBN and the coupled spin and valley indexes in monolayer transition metal dichalcogenide (TMD). **b** Polarization-resolved EL spectra under ±1.8 T out-of-plane magnetic fields, showing opposite helicity. **c** The reflective magnetic circular dichroism (RMCD) signals as a function of magnetic fields for a bilayer CrI₃/hBN/WSe₂ device. The spin switching for each

layer is sketched. The red and blue arrows indicate the spin-up and spin-down directions. The up and down indicates the magnetic field sweeping directions. **d** The corresponding extracted EL helicity as a function when sweeping the magnetic field. **e** The RMCD signals and **f** corresponding EL helicity of a trilayer CrI₃/hBN/WSe₂ device as a function of magnetic fields.

magnetic field of 2 T. Subsequently, we swept the back gate voltage while maintaining the system at 0.8, 0.71, and 0.5 T, corresponding to traces 1 to 3 in Fig. 4b, respectively. When at magnetic fields (0.8 T and 0.5 T) away from the spin-flip field, the magnetization remains in ferromagnetic and antiferromagnetic states, respectively, as shown in the RMCD measurements. Near the spin-flip field (trace 2), a repeatable switching between the ferromagnetic and antiferromagnetic states can be achieved, consistent with previous reports^{16,17}. The measured EL helicity shows corresponding repeatable switching between 7% and 21% (Fig. 4c), with switching gate voltage hysteresis similar to that observed in RMCD. We note that the incomplete AFM to FM switching here is due to the limited back gate voltages applied in this device. Alternatively, we also examined the switching capability with a trilayer CrI₃ device (Fig. 4d). The device was initially prepared at 2 T and then subjected to a fixed magnetic field just below its coercive force at -0.68 T. As the gate voltage scanned from negative to positive values, it induces a sign switch in the magnetism of CrI₃ (Fig. 4e) because of the decrease in the spin-flip field. Notably, this is a one-time-only switching event, as

the device remains in the negative sign state afterward due to it being the low-energy state under a negative magnetic field. Due to the spin reversal in CrI₃, it thus gives rise to a sign reversal in the EL helicity that is triggered by electrical signals, as shown in Fig. 4f. In addition, we investigated the repeatable switching behavior near the spin-flip transition field of 1.73 T, as shown in Supplementary Fig. 8.

Discussion

In conclusion, we showed robust spin-LED device operation composed of CrI₃/hBN/WSe₂ van der Waals heterostructures, where the spin-polarized carriers tunneled through the CrI₃/hBN layer and resulted in valley polarized and circularly polarized light emission. A close-to-unity spin transfer efficiency was achieved with our tunneling contacts. Importantly, we demonstrate an effective modulation and control of EL helicity through electrical signals due to the electrical tunability of magnetization in CrI₃. Our results provide an approach to having on-demand, electrically tunable helicity in 2D spin-LED, opening up directions to combine optoelectronics, spintronics, valleytronics, and advanced imaging.

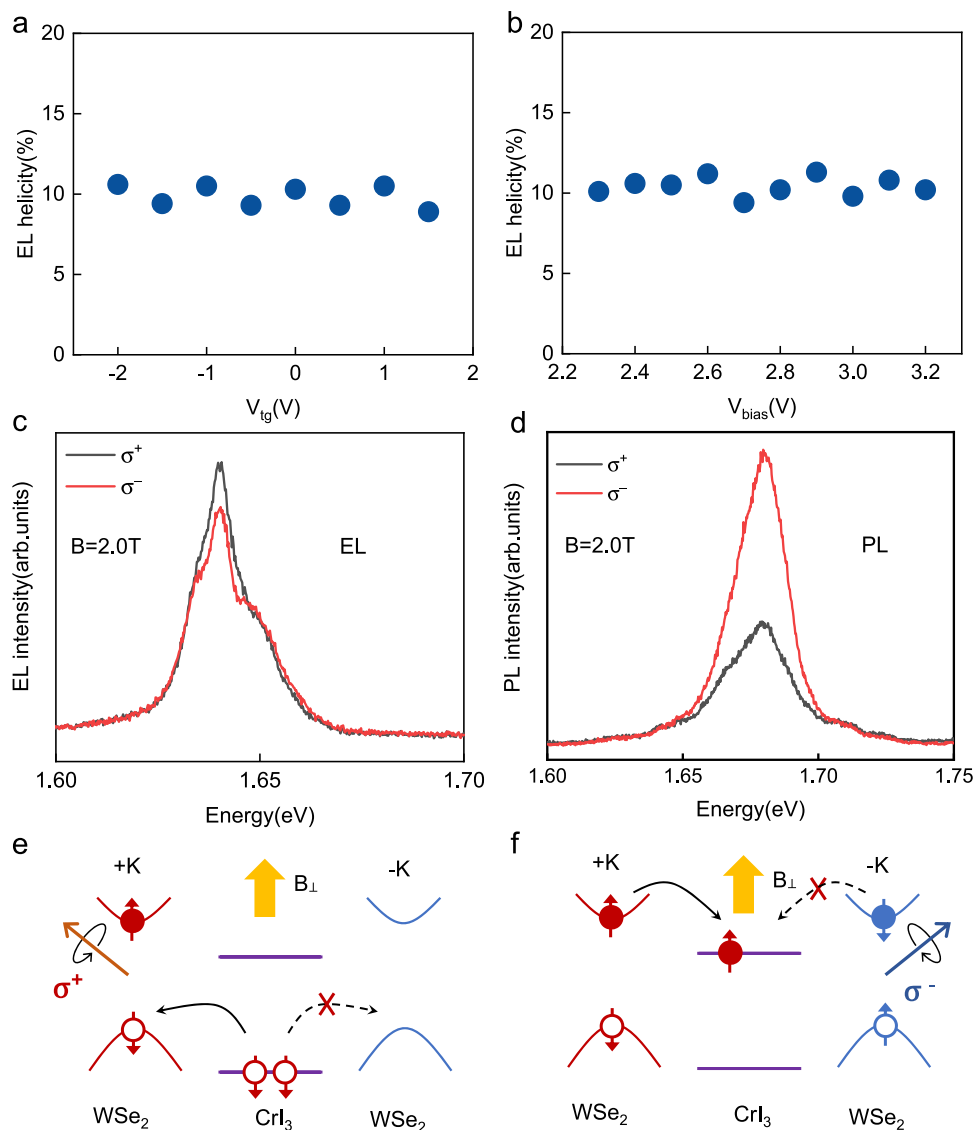


Fig. 3 | Characterization of EL helicity. **a** The evolution of EL helicity (bilayer CrI₃/hBN/WSe₂) under different V_{tg} , measured under 2 T out-of-plane magnetic field and with $V_{bias} = 2.5$ V. **b** EL helicity dependence when varying V_{bias} (after reaching the EL threshold conditions), as measured with 2 T out-of-plane field and $V_{tg} = 1$ V. **c**, **d** compares the circular polarization of the EL and PL signals at 2 T magnetic field. The PL was measured at a WSe₂/CrI₃ heterostructure region without hBN barrier, excited by linearly polarized 633 nm laser. The EL spectra were measured in a CrI₃/

hBN/WSe₂ device. EL and PL possess opposite circular polarizations. **e** The exemplary schematics illustrate the spin-polarized carrier injection process, where the spin polarization results in K valley and σ^+ EL emission. The solid and dashed arrows indicate the allowed and forbidden carrier injection. B_{\perp} represents the out-of-plane magnetic field. **f** Under the same CrI₃ spin alignment, the interlayer charge transfer favors the quenching of K valley electrons and therefore results in a higher -K exciton population and σ^- PL emission.

Methods

Crystal growth

CrI₃ single crystals were grown by the chemical vapor transport method. Chromium powder (99.99% purity) and iodine flakes (99.999%) in a 1:3 molar ratio are put into a silicon tube with a length of 200 mm and an inner diameter of 14 mm. The tube was pumped down to 0.01 Pa and sealed under vacuum, and then placed in a two-zone horizontal tube furnace. The two growth zones are raised slowly to 903 and 823 K for two days and are then held there for another seven days. Shiny, black, plate-like crystals with lateral dimensions of up to several millimeters can be obtained from the growth. In order to avoid degradation, the CrI₃ crystals are stored in an inert-gas glovebox.

Device fabrication

The few layer graphite, hBN, bilayer/trilayer CrI₃ and monolayer WSe₂ were first mechanically exfoliated from bulk crystals and identified by

their color contrast under an optical microscope. The heterostructure was built by using the dry transfer technique with a PC stamp²⁶ and released onto a substrate with pre-patterned gold electrodes. The transfer steps were performed in a nitrogen-filled glove box.

Optoelectronic measurements

The devices were mounted onto a 3D piezoelectric stage in an optical cryostat (attoDry1000) with a base temperature of 4 K. The cryostat was equipped with a superconducting solenoid magnet, which can supply a magnetic field from -9 T to 9 T. For EL and PL measurements, the emission was collected by an objective lens with a numerical aperture of 0.82 and detected by a grating spectrometer and CCD (Princeton Instruments SpectraPro HRS300 + PIXIS). The polarization of the emission was measured by using a $\lambda/4$ plate followed by a polarizer. For PL measurement, the sample was excited by a 633-nm continuous wave laser with a focal spot diameter ~ 1 μ m.

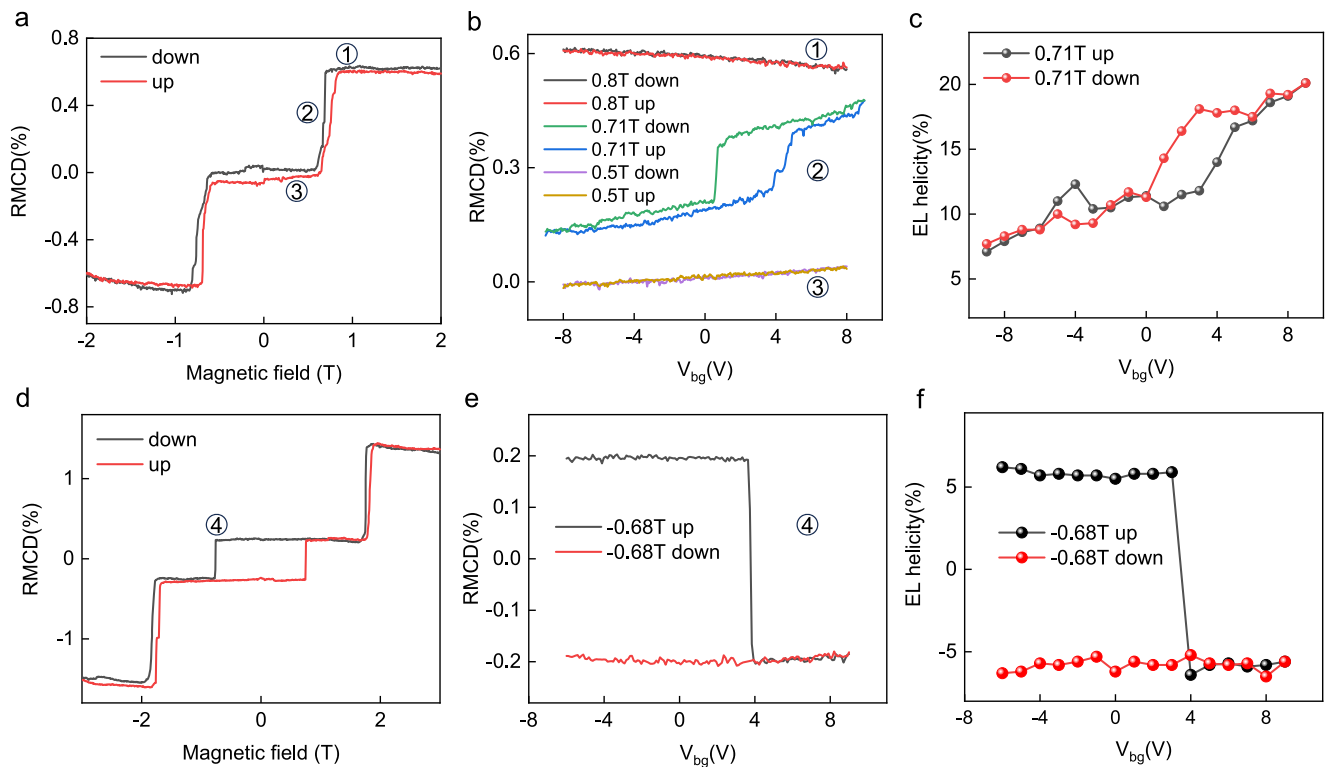


Fig. 4 | Electrical switching of EL helicity. a RMCD of bilayer CrI_3 as a function of magnetic field under zero back gate voltage at 4 K. **b** Back gate voltage control of RMCD of bilayer CrI_3 under different V_{bg} sweeping cycles. The sample was prepared in the “up” state by a magnetic field at 2 T and then biased at 0.8, 0.71 and 0.5 T corresponding to traces 1 to 3 in **a** and **b**, respectively. The up and down in **b** indicates the sweeping direction of V_{bg} . **c** The repeatable switching of EL helicity

when varying the back gate voltage at a fixed 0.71 T, which corresponds to trace 2 position in **a** and **b**. **d** RMCD of trilayer CrI_3 as a function of magnetic field under zero back gate voltage at 4 K. **e** Back gate voltage control of RMCD of trilayer CrI_3 . The sample was prepared by a magnetic field first at 2 T and then biased at -0.68 T (trace 4). **f** The EL helicity of the corresponding trilayer CrI_3 device when varying V_{bg} at a fixed -0.68 T (trace 4 position).

RMCD measurements

For RMCD measurements, the 633-nm continuous wave laser was used. The laser was modulated at 50 kHz between the left and right circular polarization using a photoelastic modulator (Hinds PEM). The reflected light was focused onto a photodiode. The RMCD was determined as the ratio of the a.c. component of the photodiode signal measured by a lock-in amplifier at the polarization modulation frequency and the d.c. component of the photodiode signal measured by an oscilloscope.

Data availability

The data that support the findings of this study are available within the paper and its Supplementary Information. Additional data are available from the corresponding authors upon request.

References

- Žutić, I., Fabian, J. & Das Sarma, S. Spintronics: Fundamentals and applications. *Rev. Mod. Phys.* **76**, 323–410 (2004).
- Fiederling, R. et al. Injection and detection of a spin-polarized current in a light-emitting diode. *Nature* **402**, 787–790 (1999).
- Ohno, Y. et al. Electrical spin injection in a ferromagnetic semiconductor heterostructure. *Nature* **402**, 790–792 (1999).
- Nishizawa, N., Nishibayashi, K. & Munekata, H. Pure circular polarization electroluminescence at room temperature with spin-polarized light-emitting diodes. *Proc. Natl Acad. Sci.* **114**, 1783–1788 (2017).
- Yang, Y., da Costa, R. C., Smilgies, D.-M., Campbell, A. J. & Fuchter, M. J. Induction of Circularly Polarized Electroluminescence from an Achiral Light-Emitting Polymer via a Chiral Small-Molecule Dopant. *Adv. Mater.* **25**, 2624–2628 (2013).
- Kim, Y.-H. et al. Chiral-induced spin selectivity enables a room-temperature spin light-emitting diode. *Science* **371**, 1129–1133 (2021).
- Li, J.-X. et al. Electric control of valley polarization in monolayer WSe_2 using a van der Waals magnet. *Nat. Nanotechnol.* **17**, 721–728 (2022).
- Ye, Y. et al. Electrical generation and control of the valley carriers in a monolayer transition metal dichalcogenide. *Nat. Nanotechnol.* **11**, 598–602 (2016).
- Farshchi, R., Ramsteiner, M., Herfort, J., Tahraoui, A. & Grahn, H. T. Optical communication of spin information between light emitting diodes. *Appl. Phys. Lett.* **98**, <https://doi.org/10.1063/1.3582917> (2011).
- Jan, C.-M., Lee, Y.-H., Wu, K.-C. & Lee, C.-K. Integrating fault tolerance algorithm and circularly polarized ellipsometer for point-of-care applications. *Opt. Express* **19**, 5431–5441 (2011).
- Chen, C. et al. Tomographic reconstruction of circularly polarized high-harmonic fields: 3D attosecond metrology. *Sci. Adv.* **2**, e1501333 (2016).
- Wang, G. et al. Colloquium: Excitons in atomically thin transition metal dichalcogenides. *Rev. Mod. Phys.* **90**, 021001 (2018).
- Mak, K. F. & Shan, J. Photonics and optoelectronics of 2D semiconductor transition metal dichalcogenides. *Nat. Photonics* **10**, 216 (2016).
- Gibertini, M., Koperski, M., Morpurgo, A. F. & Novoselov, K. S. Magnetic 2D materials and heterostructures. *Nat. Nanotechnol.* **14**, 408–419 (2019).
- Gong, C. & Zhang, X. Two-dimensional magnetic crystals and emergent heterostructure devices. *Science* **363**, eaav4450 (2019).

16. Huang, B. et al. Electrical control of 2D magnetism in bilayer CrI₃. *Nat. Nanotechnol.* **13**, 544–548 (2018).
17. Jiang, S., Li, L., Wang, Z., Mak, K. F. & Shan, J. Controlling magnetism in 2D CrI₃ by electrostatic doping. *Nat. Nanotechnol.* **13**, 549–553 (2018).
18. Jiang, S., Shan, J. & Mak, K. F. Electric-field switching of two-dimensional van der Waals magnets. *Nat. Mater.* **17**, 406–410 (2018).
19. Rashba, E. I. Theory of electrical spin injection: Tunnel contacts as a solution of the conductivity mismatch problem. *Phys. Rev. B* **62**, R16267–R16270 (2000).
20. Zhong, D. et al. Van der Waals engineering of ferromagnetic semiconductor heterostructures for spin and valleytronics. *Sci. Adv.* **3**, e1603113 (2017).
21. Huang, B. et al. Layer-dependent ferromagnetism in a van der Waals crystal down to the monolayer limit. *Nature* **546**, 270 (2017).
22. Yu, T. & Wu, M. W. Valley depolarization due to intervalley and intravalley electron-hole exchange interactions in monolayer MoS₂. *Phys. Rev. B* **89**, 205303 (2014).
23. Zhong, D. et al. Layer-resolved magnetic proximity effect in van der Waals heterostructures. *Nat. Nanotechnol.* **15**, 187–191 (2020).
24. Lyons, T. P. et al. Interplay between spin proximity effect and charge-dependent exciton dynamics in MoSe₂/CrBr₃ van der Waals heterostructures. *Nat. Commun.* **11**, 6021 (2020).
25. Zhang, X.-X. et al. Gate-tunable spin waves in antiferromagnetic atomic bilayers. *Nat. Mater.* <https://doi.org/10.1038/s41563-020-0713-9> (2020).
26. Wang, L. et al. One-Dimensional Electrical Contact to a Two-Dimensional Material. *Science* **342**, 614 (2013).

Acknowledgements

X.-X.Z. acknowledge the support from the Department of Energy (DOE) award DE-SC0022983. This work was partly conducted at the Research Service Centers of the Herbert Wertheim College of Engineering at the University of Florida. H.C.L. was supported by Beijing Natural Science Foundation (Grant No. Z200005), National Key R&D Program of China (Grants Nos. 2022YFA1403800, 2023YFA1406500), and National Natural Science Foundation of China (Grants Nos. 12274459).

Author contributions

X.-X.Z. and J. D. designed the study. J.D. and T.W. fabricated the device and performed the measurements. K.W. and T.T. grew the bulk hBN crystals. S.Y. and H.C.L. grew the bulk CrI₃ crystals. X.-X.Z. and J.D. wrote

the manuscript. All authors discussed the results and commented on the manuscript.

Competing interests

The authors declare no competing interests.

Additional information

Supplementary information The online version contains supplementary material available at <https://doi.org/10.1038/s41467-024-51287-9>.

Correspondence and requests for materials should be addressed to Xiao-Xiao Zhang.

Peer review information *Nature Communications* thanks the anonymous reviewers for their contribution to the peer review of this work. A peer review file is available.

Reprints and permissions information is available at <http://www.nature.com/reprints>

Publisher's note Springer Nature remains neutral with regard to jurisdictional claims in published maps and institutional affiliations.

Open Access This article is licensed under a Creative Commons Attribution-NonCommercial-NoDerivatives 4.0 International License, which permits any non-commercial use, sharing, distribution and reproduction in any medium or format, as long as you give appropriate credit to the original author(s) and the source, provide a link to the Creative Commons licence, and indicate if you modified the licensed material. You do not have permission under this licence to share adapted material derived from this article or parts of it. The images or other third party material in this article are included in the article's Creative Commons licence, unless indicated otherwise in a credit line to the material. If material is not included in the article's Creative Commons licence and your intended use is not permitted by statutory regulation or exceeds the permitted use, you will need to obtain permission directly from the copyright holder. To view a copy of this licence, visit <http://creativecommons.org/licenses/by-nc-nd/4.0/>.

© The Author(s) 2024, corrected publication 2024